EUROPEAN FUSION DEVELOPMENT AGREEMENT

EFDA–JET–PR(03)28

M. Mattioli, K.B. Fournier, I. Coffey, M. Finkenthal and M. Valisa
and JET EFDA contributors

Experimental and Simulated M-Shell Nickel Spectra in the 14.4 -18.0nm Region from Magnetic Fusion Devices

Experimental and Simulated M-Shell Nickel Spectra in the 14.4 -18.0nm Region from Magnetic Fusion Devices

M. Mattioli[1], K.B. Fournier[2], I. Coffey[3], M. Finkenthal[4, 5] and M. Valisa[1]
and JET EFDA contributors*

[1]Consorzio RFX, Corso Stati Uniti 4, Padova I-35127
[2]Lawrence Livermore National Laboratory, PO Box 808, L-41 Livermore, Ca 94550, USA
[3]Queen's University, Belfast BT7 1NN, UK
[4]Racah Institute of Physics, Hebrew University, Jerusalem, Israel
[5]Plasma Spectroscopy Group, the Johns Hopkins University, Baltimore, Maryland 21918, USA
** See annex of J. Pamela et al, "Overview of Recent JET Results and Future Perspectives", Fusion Energy 2000 (Proc. 18th Int. Conf. Sorrento, 2000), IAEA, Vienna (2001).*

Preprint of Paper to be submitted for publication in
Physica Scripta

ABSTRACT.

Experimental M-shell nickel spectra in the 14.4-16.5nm region from the JET tokamak (both on divertor and limiter configurations) and from the reversed field pinch RFX have been simulated. These spectra include lines from five ionisation states, namely from Ni^{10+} K-like to Ni^{13+} P-like ions. For the JET limiter configuration the spectrum upper upper limit was higher (18.0 nm) and lines from Ni^{14+} Si-like ions were also observed CollisionalRadiative (CR) models have been built for these six Ni ions, considering electron collisional excitation and radiative decay as the populating processes of the excited states. These models give Photon Emission Coefficients (PECs) for the emitted lines at electron density (n_e) and temperature (T_e) values corresponding to the experimental situations. Impurity modelling is performed using a 1-D impurity transport code, calculating the steady state radial distribution of the Ni ions. The Ni line brightnesses are evaluated in a post-processing subroutine and simulated spectra are obtained. The partial spectra corresponding to a single ionisation degree, in absence of blendings, depend only of the Te and ne values in the emitting shells of the ionisation states considered. On the other hand, the superposition of the these spectra depends on the experimental conditions, as a consequence of the fact that the ion charge distribution depends not only on the radial profiles of T_e and n_e, but also on the chosen ionisation and recombination rate coefficients and on the radial profiles of the impurity transport coefficients in the region of the emitting shells. For each experimental spectrum a few simulations are presented, since a unique choice has not been found by selecting the input parameters of the transport code. Since the aim of the paper is an investigation of the atomic physics of the M-shell ions, this section on the plasma physics phenomena is purposely quite limited. Various simulations are, nevertheless, necessary to determine the electron density and temperature values in the emitting shells and to show the influence of line blendings on the single ionisation degree spectra. The single ionisation degree spectra are then compared with the predictions. For the considered n_e range the PECs can be considered independent of n_e. There is a their T_e dependence, but it is much reduced when considering line ratios and the spectral fits done are actually a comparison of line ratios. The global agreement found between experimental and simulated single ionisation degree spectra give confidence on the atomic data used to build the required CR models.

1. INTRODUCTION

Intrinsic and/or purposely seeded impurities are always present in Magnetic Confinement Fusion (MCF) devices. Spectrometers observing plasma emission from the visible wavelength range up to the X-ray range are installed on these devices. Most of the work is usually dedicated to the determination of both the plasma chemical composition (i.e., the identification of the impurity elements and the evaluation of their concentration) and the impurity transport coefficients. For this purpose only a few selected strong lines are considered and are simulated using impurity ion transport codes (see, e. g., Ref. [1]). Until recently simulation of full spectra were less frequent with the exception of K-shell spectra (i.e., the satellite spectra associated with the He-like resonance lines)

for elements ranging from Ar to Ni (see, e. g., the rewiew of Ref. [2]). Full simulation in the XUV range of both n = 2 to n = 2 and n = 3 to n = 2 L-shell Ne and Ar spectra have been recently published [3-5]. As discussed in Ref. [6], the analysis of spectra emitted by hot and well diagnosed MFC plasmas is important since it touches atomic physics issues that are required for simulation codes to be used in the analysis of high spectral resolution data from X-ray telescopes. Spectral diagnostics are used to measure the physical conditions of the observed objects, i.e., electron temperature, electron density and elemental abundances. An example of such an anlysis of experimental spectra can be found in Ref. [7], in which electron density sensitive XUV line ratios from L-shell iron ions in the FTU tokamak were studied. These observations, as explained in Ref. [7], are directly applicable to recent astrophysical measurements and confirm observations of surprisingly high electron densities reported in astrophysical papers [8, 9].

M-shell spectra are also of astrophysical interest and it is then useful to have the possibility to verify in MCF devices the proposed atomic physics models. This has been done also on the FTU tokamak for a n = 3 to n = 3 spectrum of iron ions [10]. The observed charge states spanned from K-like Fe^{7+} to Si-like Fe^{12+} ions and the fractional ion abundances were found by fitting the model spectra to the measured spectrum. In this paper similar experimental M-shell Ni spectra are reported. We must point out here that in Ref. [10] analysis of astrophysical M-shell iron spectra are quoted, whereas, to the best of our knowledge, no corresponding nickel spectra have been observed. The Ni spectra have been obtained in two different experimental conditions on the Jet tokamak and also in a single experimental condition on the reversed field pinch (RFP) RFX. The spectra are similated using an impurity transport simulation code, which describes ionisation, recombination and radial transport of the ions of a given impurity species. It requires as input data the radial profiles of the electron temperature $T_e(r)$ and of the electron density $n_e(r)$, needed to evaluate the ionisation and recombination rate coefficients, and two transport coefficients (a diffusion coefficient D(r) and a convection velocity V(r). Difficulties were faced to get a satisfactory simulation of the experimental spectra. The first one is related to the low ionisation degree of the involved ions, their temperature of maximum abundance at ionisation equilibrium (IE) being in the 100eV range. For low ionisation ions of medium atomic number elements like Ni it has not been possible to obtain from the published literature a unique choice of assessed and/or reliable ionisation and recombination rate coefficients. Moreover, in the Jet tokamak their emitting shells are at the extreme periphery near the Last Closed Flux Surface (LCFS) or outside in the Scrape-Off Layer (SOL). Unfortunately, for the discharges during which the spectra were obtained no peripheral $T_e(r)$ and $n_e(r)$ profiles were available and only extrapolations from inside the LCFS were possible. On the other hand, on RFX, as a consequence of the maximum $T_e(r)$ of the order of 200eV, the emitting shells of the involved ions are located in a plasma region with measured Te and ne values. But it will appear that, even in this case, it has not been possible to obtain a satisfactory unique spectral simulation.

The aim of this paper is an investigation of the physics of the M-shell Ni ions rather than the impurity Ni ion behaviour in MCF devices. Our previous work on Ar and Ne spectra [3-5], confirmed

by the analysis to be reported in this paper, has indicated that the parts of the spectra corresponding to a single ionisation degree in absence of blendings depend only of the Te and ne values in the emitting shells of the ionisation states considered.. The Collisional Radiative (CR) models constructed to simulate ion emission can, therefore, be studied individually and their validity established. Consequently, comparison of the experimental single ionisation degree partial spectra with the predicted ones is possible, in spite of a unsatisfactory 'global' simulation of the experimental spectra. Indeed, the relative amplitudes of the 'independent' spectra are determined by the ion charge state distribution, that depends not only on the radial profiles of T_e and n_e, but also on the chosen ionisation and recombination rate coefficients and on the radial profiles of the impurity transport coefficients in the region of the emitting shells of the ionisation states considered.

The paper is organised as follows. In section 2 the experimental conditions are described along with examples of the experimental spectra, in which the strongest lines are identified, including those emitted by other intrinsic elements. Two spectra are presented for JET, the first one for a diverted discharge and a second one for a limiter discharge, both with supplementary heating. For RFX the spectrum shown has been obtained in an ohmic discharge. CR models have been constructed for Ni ions from K-like Ni^{9+} to Si-like Ni^{14+} ions, considering electron collisional excitation and radiative decay, as the populating processes of the excited states. In section 3, Photon Emission Coefficients (PECs) are given for the lines emitted by the excited levels for T_e and n_e values corresponding to experimental situations of the MFC devices. Comparison of these PECs with published literature is presented, this being only possible for Cl-like $Ni1^{1+}$ [11] and S like Ni^{12+} [12]. Impurity modelling, briefly described in section 4, is performed with a one-dimensional (1D) impurity transport code, calculating the steady-state radial distribution of the Ni ions. The Ni line brightnesses are evaluated in a post-processing subroutine to simulate the spectra. The proposed ionisation and recombination rate coefficients are presented in this section, along with the corresponding ion charge state distribution at IE. In section 5 simulated spectra are presented. For each simulation the best fit is done on the peaks of the strongest lines of the Ni ionisation degrees contributing to the features of the detected spectra.. The 'best' spectra are the ones with the lowest estimated sample deviation at the spectral peaks. For each experimental spectrum a few simulations are presented, since a unique choice has not been found by selecting the input parameters of the transport code, namely, the $T_e(r)$ and $n_e(r)$ profiles, the two transport coefficients and the ionisation plus recombination rates. Since the aim of the paper is an investigation of the atomic physics of the M-shell ions, this section on the MCF-specific relevant plasma physics phenomena is purposely quite limited. Various simulations are, nevertheless, necessary to determine the n_e and T_e values in the emitting shells and to show the influence of line blendings on the single ionisation degree spectra.

The comparison of the single ionisation degree spectra with the predictions is presented in section 6. For the considered n_e range the PECs can be considered independent of n_e. There is a their T_e dependence, but it is much reduced when considering line ratios and the spectral fits done are actually a comparison of line ratios. Moreover, the range of T_e values is quite limited, since for all

ions the simulated emissivities are at radii where Te is slightly higher than the temperature of maximum abundance at IE. Finally, concluding remarks are given in section 7.

2. EXPERIMENTAL DATA

The plasma of the JET tokamak with the divertor installed has an approximately elliptical cross section (minor radius a = 0.95m, plasma half height b = 1.75m, major radius R_0 = 2.85m, plasma elongation b/a = 1.85), a maximum plasma current Ip = 6MA and toroidal magnetic field (at R_0) B_t = 3.8T. Neutral beam injection (NBI), Ion Cyclotron Resonance Heating (ICRH) and Lower Hybrid Current Drive (LHCD) are available as supplementary heatings. XUV spectra are observed with the Schwob-Fraenkel extreme grazing incidence vacuum spectrometer, which is equipped with two microchannel plate detectors and views the plasma along a central line of sight and has a Full Width Half Maximum (FWHM) resolution of 0.02nm [13]. The spectrum of Fig.1 between 14.3 and 16.5nm is the average of several spectra obtained during one second interval of a diverted H-mode discharge heated by 14 MW of NBI power, the plasma parametres being the following I_p = 1MA, B_t = 2.9T, $n_e(0) \approx 1e^{14}$ cm^{-3}; $T_e(0) \approx 10$ keV. The strongest Ni lines are identified along with the O VI 15 nm line.

The n_e and T_e radial profiles are obtained by Lidar Thomson scattering. Unfortunately, the available data don't reach the LCFS, they have been extrapolated to values quite near the ones obtained at the LCFS in recent diverted H-mode dicharges, when the peripheral Lidar system was operating [14, 15]. In the SOL, to simulate the variations of the profiles outwards, we suppose, approximately, an exponential decrease with decay lengths to be adjusted to optimise the simulation results.

A second experimental JET spectrum (also average of several spectra obtained during one second interval of a L-mode discharge) is shown in figures 2. This spectrum extends further up to a maximum wavelength of 18.0nm, so more Ni XIV and Ni XV lines are observed. This spectrum has been obtained prior to the divertor installation, when the plasma size was reduced. At that time the nominal plasma parameters were: minor radius a = 1.25m, major radius R_0 = 2.95m, plasma elongation = 1.6, a maximum plasma current I_p = 7MA and toroidal magnetic field (at R_0) B_t = 3.4 T. The spectrum of figure 2 has been obtained in a plasma heated by 7 MW of ICRH power with the following parameters: I_p = 5MA, B_t = 3.3T, $n_e(0) \approx 0.5$ e^{14} cm^{-3}; $T_e(0) \approx 3.8$keV. The strongest Ni lines are identified along with intrinsic C, O and Cr lines. Tables with the lines identified in similar Jet predivertor plasmas can be found in Ref. [16].

Also for this discharge the n_e and T_e radial profiles are obtained by Lidar Thomson scattering, but the available data don't reach the LCFS. In the pre-divertor conditions the plasma was limited by several discrete carbon limiters and the inconel walls were partially covered on the inner side by carbon tiles. Langmuir probes showed that the SOL was quite thin with decay lengths in the cm range, with probe T_e values at the LCFS lower than 100eV, i. e., as it will be shown in section 4, lower than the temperatures of maximum abundance at IE of the considered Ni ions. It seems therefore justified to neglect the SOL by taking the last mesh at the LCFS radius at 1.2m, The

Thomson scattering data were extrapolated to the LCFS with limit T_e and n_e values near the probe values [17]. Optimisation of the simulation required both profiles to be relatively flat in the last 50mm. RFX is a large reversed field pinch (minor radius $a_L = 0.46$ m, major radius $R = 2.0$m) designed to operate with a plasma current I_p up to 2MA (currently operated with $I_p = 0.5$-1MA). The central toroidal magnetic field is 0.5-1 T. No additional heating system is installed, as is common to RFP devices. The inconel vacuum vessel is almost completely covered with carbon tiles; carbon and oxygen are, therefore, the main impurities, metallic impurities being reduced to very low levels. Also in this device XUV spectra are observed with a Schwob-Fraenkel spectrometer, An example of Ni spectrum in the same wavelength range as the Jet spectrum of figure 1 is shown in figure 3. The $n_e(r)$ and $T_e(r)$ profiles are obtained, respectively, by a multichord CO_2 laser interferometer and by a Thomson scattering system complemented by a Si-Li X-ray detector and a double-filter soft X-ray monitor [18].

3. ATOMIC STRUCTURE CALCULATIONS AND *COLLISIONAL-RADIATIVE MODELS*

We describe in this section how the (steady-state) Collisional-Radiative (CR) Photon Emission Coefficients (PECs) have been computed for Si-like to K-like nickel ions. Each ion has been treated independently from the others. Ionization and recombination into and out of the ground and excited energy levels of each ion have been ignored, as well as ion collisions with large rate coefficients when close levels are involved. The steady state level populations are found by inverting the full CR rate matrix for each ion [19].

The atomic data used in constructing the emission models for each ion in the present work are generated from *ab initio* atomic structure calculations with the Hebrew University Lawrence Livermore Atomic Codes (HULLAC). The atomic structure calculations are performed with the graphical angular momentum coupling code ANGLAR [20] and the fully relativistic parametric potential code RELAC [21, 22]. For a given ion, RELAC solves the Dirac equation by varying an analytic ionic potential in order to minimize the average energy of a configuration (or of a set of configurations). Once the zeroth order wavefunctions minimized, the configuration-average energy of each configuration (or of set of configurations) have been found, and RELAC calculates the multi-configuration, intermediate-coupling energy eigenvalues of the fine structure levels. Inclusion of higher order energy corrections (Lamb shift, Breit interaction, etc.) is discussed elsewhere [19]. Radiative transition rates are then computed for any requested multipole operator in the Coulomb gauge (thus, in the dipole velocity form of the transition operator matrix element) and explicitly includes retardation effects. RELAC's full multiconfiguration wavefunctions are used to compute the radiative transition rates; therefore, configuration mixing affects the calculated oscillator strengths.

RELAC's wavefunctions are used in the quasi-relativistic code CROSS [23] to compute collisional-excitation collision strengths between all the levels of a given ion in the Distorted-Wave Approximation (DWA). CROSS is able to accomplish this by using the factorization theorem of

Bar-Shalom, Klapisch and Oreg in conjunction with a semiempirical interpolation scheme [23] for the radial integrals required by the "factored" collision operator. The distorted-wave cross sections are then integrated over a Maxwellian distribution of free electron energies to determine the final impact excitation rate coefficients. In our previous work [3, 7, 8], for certain iso-electronic sequences, it was necessary to augment DWA electon-impact collision strengths for transitions between closely-spaced, fine-structure energy levels near to the ground level with *R*-matrix data in order to achieve agreement with measured spectral line strengths. In the present work, we have compared our DWA collision rates for NiXII with the recent *R*-matrix data of Matthews et al. [24], and find agreement between 1 – 15% (generally better than 10%) for strong, electric-dipole allowed transitions between levels in the $n = 3$ shell, and within a factor of 2 – 10 for optically forbidden transitions. The effect on three temperaturesensitive line ratios of replacing the collision rates among the fine-structure levels of the first two configurations in NiXII with the data from [24] is shown in Appendix A.

If n_j is the relative population of level j, the resulting photon emission coefficient (PEC) for a given transition between level j and i is

$$P_{j,i} = \frac{n_{j,}}{N_e} \sum A_{j,i} \tag{1}$$

where the sum over the *A*-rates is over all multipoles connecting the two levels j and i in question, and the electron density is divided out of the model. The resulting units are photons m^3 sec^{-1}. The PECs have been calculated on a 8*8 grid for ne from $1e^{18}$ to $3e^{20}$ m^{-3} and for Te ranges spanning around the temperatures of maximum abundance (roughly from one third to three times), ranges corresponding to experimental situations of the MFC devices. In the considered ranges the PECs $P_{j,i}$ are increasing functions of T_e (generally with a weaker dependence when considering line ratios) and (when multiplied by Ne since Ne is divided out of the model) practically independent of ne, except for some lines at $n_e = 1e^{18}$ m^{-3}, when differences of the order of 10% are are observed (see an example for Ni XII in Appendix A).

In Appendix A our PECs for Ni XII and Ni XIII are compared with the ones reported, respectively, in Refs [11] and [12]. In the same Appendix a few considerations on the effect of ion collisions on level population are also included.

The energy level values were implemented from the assessed spectral data by Shirai et al. [25], from the Nist database [26] and from the Kelly's book available on the web [27]. Also three Fawcett's papers with atomic data for Ni XII' – XIII – XIV were used in this context [28-30]. With one exception for Ni XIII, the lines included are the ones with experimental values reported in these references. Their wavelengths and energy levels involved in the transitions are given in Appendix B. For a few energy levels found in the quoted references we don't find agreement with our experimental data, we will make the corrections and we will discuss this point in section 6 when considering the individual ion spectra.

4. IMPURITY MODELLING

The impurity transport simulation code describes in cylindrical geometry, ionisation, recombination and radial transport of the ions of a given atomic species. The following system has to be solved:

$$\partial n_z/\partial t = -(1/r)\,[\partial(r\Gamma_z)/\partial r] + n_e\,(n_{z-1}\,S_{z-1} - n_z S_z + n_{z+1}\,\alpha_{z+1} - n_z\,\alpha_z \quad z = 1, 2, ...Z_N \qquad (2)$$

where Γ_z is the radial particle flux density (positive when directed outwards) of the ions of charge z of the considered atomic species of nuclear charge Z_N. n_z is the corresponding ion density. S_z, α_z are, respectively, for the ions of charge z the ionisation rate coefficients and the radiative (RR) plus Dielectronic Recombination (DR) rate coefficients. In the reported simulations, system (2) neglects two processes sometimes included: the Charge-Exchange (CX) recombination with neutral hydrogen isotopes and an impurity confinement time τ_p different from infinity for particle transport along the field lines in the SOL. The former process is usually neglected, unless there is experimental evidence of a large amount of neutral hydrogen isotopes at the periphery (e.g., because of a strong gas puffing).

For the needed atomic rate coefficients two sets of data are available. Recently, Mazzotta et al. [31] presented a critical review of the ionisation and recombination rate coefficients for all the elements up to Ni. New ionisation balances were evaluated and compared with the literature. In previous simulations with our simulation code, on the other hand, were included the ionisation rate coefficients proposed by Pindzola et al [32]. They were performed in the distorted wave approximations and for 8 ions up to Ni^{14+} experiments and theory were compared. Recently, Cherkani-Hassani et al. [33] published new experimental data for $Ni^{10+,\ 11+,\ 13+,\ 15+}$ which showed satisfactory agreement with the distorted wave calculations by Pindzola et al. [32], with the exception of Ni^{10+}, when the experiment underestimates the calculations by about 30% at the peak of the cross section. Since the authors claim that their beam was strongly dominated by metastable configuration population, we don't feel necessary to modify for this ion the distorted wave value.

As far as DR rate coefficients are concerned, specific calculations are available for highly ionised ions starting from recombining Mg-like ions. For less ionised ions (the ones considered in this paper) data are based on the well known Burgess-Merts' formula including a $\Delta n = 0$ and a $\Delta n = 1$ transition, taking in the literature the needed values of the oscillator strengths and of the excitation energies.

As a consequence of different choices of these two parameters, the rate coefficients proposed by Mazzotta et al. [31] and the previously used in our transport code [34] are somehow different.

In the figure 4 the rate coefficients for ionisation Sion, for radiative recombination α_R, and for dielectronic recombination α_{DR} as functions of Te are compared for the two data from Ni^{9+} to Ni^{14+}, the solid lines referring to Ref. [31] and the dashed lines, respectively, to Ref. [32] for ionisation and Ref. [34] for recombination. Ionisation are from and recombination into the indicated ionisation degree.

For the four 'couples' of rate coefficients the fractional abundance f_z (Te) curves at IE are compared for the six ions involved in the experimental spectra in figure 5.The rate coefficients used for each kind of curve are specified in the caption.

The differences between the various f_z (T_e) curve are decreasing with increasing ionisation degree, what is expected observing the curves of figure 4, where differences in atomic data diminish with increasing Ni charge state. The influence of the four 'couples' of ionisation and recombination rate coefficients on the spectral simulations will be compared in the next section 5. Since it will appear that the DR rate coefficients from Ref. [34] give a better representation of the experimental data than the ones proposed in Ref. [31], in Appendix C fitting parameters (to be used in the same formula as in Ref. [31]) are given for low ionisation Ni ions up to recombining Al-like Ni^{15+} ions.

The impurity flux density Γ_z is expressed as the sum of both diffusive and inward convective terms

$$\Gamma_z(r) - -D(r)\, \partial n_z(r)/\partial r_z - V(r)\, n_z(r) \qquad (3)$$

where D(r) and V(r) are the radially dependent diffusion coefficient and inward convection velocity, respectively, both taken independent of the charge z of the ions. In the simulations of the following section, in view of optimising them, various D(r) and V(r) curves will be used.

A post-processing subroutine evaluates the brightnesses of the considered Ni lines and, successively, the simulated spectrum is obtained taking a Gaussian instrumental function with FWHM equal to 0.02nm.

5. SIMULATION OF THE M-SHELL SPECTRA

As already said in the introduction, the aim of the paper is an investigation of the atomic physics of the M-shell ions, i.e., the simulation of the single ionisation degree spectra. Various simulations are, nevertheless, necessary to determine the n_e and T_e values in the emitting shells (then the choice of the PEC values) and to show the influence of line blendings on the single ionisation degree spectra. Given all the uncertainties in experimental data discussed on section 2, we have tried to optimise the simulations with reasonable choices of the peripheral plasma input parameters.

For the JET divertor configuration and for RFX the experimental spectra (figures 1 and 3) span a common 14..4 – 16.5nm range. For their simulations the following procedure has been chosen: the best fit is done on the peaks of the strongest lines of the five ionisation degrees (Ni X-XIV) contributing to the features of the detected spectra (i. e., for JET, at 14..499, 14.838, 15.215, 15.773 and 16.4146 nm and, for RFX, at 14.838, 15.215, 15.417 15.773 and 15.998nm). If $sp_{exp}(\lambda)$ and $sp_{sim}(\lambda)$ are, respectively, the normalised experimental and simulated spectra, C_{mult} is a multiplicative constant, whose value is obtained by minimisation of $(\Sigma_i\, (C_{mult}\, sp_{sim}(\lambda_i) - sp_{exp}(\lambda_i))^2$ over selected lines.. The 'best' spectra are the ones with the lowest estimated sample deviation simply defined as square root of sum to be minimised.

For the JET spectra to obtain the simulations with the lowest sample deviations we varied firstly, as already said in section 2, the extrapolations of the $T_e(r)$ and $n_e(r)$ profiles from the last experimental points. For the divertor configuration a LCFS radius of 0.95 m is taken, with $T_e(r)$ and $n_e(r)$ decreasing in the 5cm SOL with decay lengths λ_T and λ_n. For the limiter configuration with a LCFS radius of 1.2m, no SOL was considered, as already justified in section 2.

In previous simulations of JET spectroscopic data, both in divertor configurations [4, 5, 35] and in limiter configurations [36], it was necessary to include both for intrinsic and injected impurities a transport barrier inside the LCFS. This is obtained by shaping either both D(r) and V(r) or just one of them in such a way as to produce what is called a peripheral barrier, as it was was first considered in Ref. [36]. There what are called diffusive (by reducing D(r)) or convective (by increasing V(r)) barriers have been compared and a range of possible transport coefficients was found, preventing to reach a final choice. In more recent simulations [4, 5, 35] diffusive barriers were considered. In the core plasma D(r) was generally found decreasing towards the plasma axis, whereas V(r) (positive then inward at the periphery) could became large in centre (indicating impurity peaking) or become negative (then outward, indicating hollow impurity profiles). For the simulations done for the present paper (considering only peripheral ions) we took the D(r) and V(r) curves used in Refs [4] and [35], changing in different trials, only D(r) in the last meshes. As a third choice of variable parametres we used the four couples of ionisation and recombination rates, already considered in the discussion of the IE curves shown in figure 5. The corresponding four simulations use the following rate coefficients, respectively, for ionisation and recombination: simulation 1 both from Refs [31], simulation 2 from Refs [32] and [31], simulation 3 from Refs [32] and [34] and simulation 4 from Refs [31] and [34],

Figure 6 shows, for the best obtained simulation of the Jet divertor spectrum (with $\lambda_T = 30$mm and $\lambda_n = 50$mm), peripheral radial profiles of a) n_e and T_e; b) D and V (same as in Ref. [35]); c) a few Ni ion densities (Ni^{9+} to Ni^{15+}) n_Z, normalized to the maximum total Ni ion density (divided by 5 in the figure); and d) the emissivities (normalised) E_{nor} of the strongest Ni X to Ni XIV lines. The vertical dashed line indicates the position of the LCFS. The data shown correspond to simulation 3, i.e., to the solid line $f_z(T_e)$ curves of figure 5. The electron temperatures at the peak ion densities are, respectively, for Ni^{9+} to Ni^{14+}: 98, 112, 145, 167 190 and 220eV. They are all quite near, but slightly larger than the corresponding T_e of maximum abundance, that would be obtained in the simulation with D(r) and V(r) approaching zero. Consequently, in the considered radial range the plasma is ionising, i. e., less ionised than at IE. But, in spite of the low ionisation potential of the considered Ni ions, the influence of recombination is not negligible.. In the accepted model of impurity 'fuelling' in MCF devices, impurity neutrals penetrate into the SOL and are progressively ionised without recombination. Moreover, figure 6 shows that the emitting shells cannot be considered single temperature shells, as implicitly assumed in Ref. [11] for the analysis of JET Ni XII line ratios. The authors of Ref. [11] use for their comparison T_e values from Langmuir probes at a non-indicated radial position, certainly in the SOL. For the considered Pulse No: 31798 they used 100eV, not much different from the value of 145eV we found in the shown simulation.

In figure 7 are shown, from top to bottom for simulation 1 to 4, the comparisons between experimental (solid line) and simulated (dashed line) spectra.

The squares of the previously defined sample deviation are, respectively, 0.042, 0.080, 0.024, 0.054. Both the numerical criterion and visual inspection of the figure indicate that, at least for this shot, the best is simulation 3 (i.e., ionisation and recombination rate coefficients, respectively, from Refs [32] and [34]). The lines without simulations obviously are not Ni lines (their identification can be found in Ref.[16]). An exception is the feature around 14.7nm, which is a Ni feature, presumably due to lower ionisation ion lines (in the tables of Ref. [25] a Ni IX is given at 14.70nm).

In all simulations performed for this shot by varying, as explained above, the various input parameters, simulation 3 was clearly always the best. We give a few examples of variation of the square of sample deviation for simulation 3. Increasing D outside the LCFS from 0.13 to 0.2 m^2/s does not modify much its value (from 0.024 to 0.026), the variation is the same by taking λ_n = 60mm, but larger (0..032) with λ_n = 40 mm. On the other hand, taking the D(r) and V(r) curves used in Refs [4] the square of the sample deviation becomes then 0.036. lT is a more critical parameters, since decreasing it to 25mm and increasing it to 40mm the squares of the samplr deviation become, respectively, 0.038 and 0.087.

The limiter plasma spectrum has been analysed in the way, but in this case the best simulation has been obtained taking the D(r) and V(r) curves used in Refs [4]. Figure 8 is the same as figure 6 also for simulation 3 found again to be the best. But, contrary to the divertor plasma, between the various combinations of the simulation parameters tested, simulation 3 was not systematically the best. As figure 2 shows, for this plasma condition the experimental spectrum spans a larger wavelength range up to 18.0nm, but above 16.5nm, i.e., the upper limit of the divertor plasma spectrum, the simulations are of 'worse' quality. We proceed by steps.

Figure 9 is the same as figure 7, with best fit to the same five lines in the same wavelength range. The square of the sample deviation are: 0.07, 0.16, 0.024 and 0.14, increasing to 0.096, 0.065, 0.055 and 0.24 using the D(r) and V(r) curves of Ref. [35]. To analyse the Ni XIV and of NI XV spectra, the spectral simulation has been extended in figure 10 up to 17.5nm and in figure 11 up to 18.0nm. In the former two lines are added to the five lines used previously for the best fit, i. e., the Ni XIV 17.137 and Ni XV 173.72 nm. In latter the Ni XV 17.927 nm line has been usad as eigth line. In figure 10 the squares of the sample deviation are: 0.19, 0.36, 0.07 and 0.15, larger than for the comparison of figures 9, but of enough good quality. They are still larger for the simulation of figure 11, namely, 0.22, 0.45, 0.14 and 0.17. Also in these two cases simulation 3 is the best.

The RFX spectrum has been simulated using the same procedure. The spectrum presented in figure 3 have been simulated with the transport coefficients found for intrinsic C and O [16] and injected Ne [5] (see, respectively, figures 7 and 10 in these references).

Figure12 is the same as figures 6 and 8 for the simulation 3, the most abundant central ions are Ni^{13+} and $Ni1^{14+}$. The total Ni ion density profile is hollow, since the convection velocity becomes outwards in the plasma core. The usual four spectral comparisons are presented in figure 13. The

square of the sample deviation are: 0.30 0.20 0.17 0.28. From these values it appears that the 'quality' of these RFX simulations is lower than for the Jet simulations. Moreover, it does not seem possible to choose between the rate coefficients, even if simulation 3 seems in all cases a little bit better

6. SIMULATION OF THE NI X TO NI XV SPECTRA

In this section we analyse the partial spectra emitted by a single ionisation degree. In Ref. [11] Keenan et al. analysed only the Ni XII spectrum, by comparing the three experimental line ratios R1, R2 and R3 with the corresponding calculated values at a single electron temperature. On the other hand, since we have done a full transport simulation of the a multi-ion spectrum, we prefer to extract from the simulations the contribution of each ionisation degree. In absence of blendings of lines from different ions, it will be possible to verify independently each CR model. We will present first these single ion spectra and then we will see how they are affected by the blendings. This procedure is facilitated by the fact that, as already mentioned, the PECs are independent of ne and increasing function of T_e. But the line ratios are quite insensitive to Te, and, independently of the analysed spectrum, each ion has maximum peak density and maximum line emissivity near (slightly higher than) the temperature of maximum abundance at IE. In figure 14 exemples of normalised single ion spectra are preseted for Ni X to Ni XV. All these spectra are the same to a few per cent for all simulations done. However, some of the spectral features are blendings of NI XIII lines. We have recalculated the single ion spectra of figure 14 by adding the simulated contributions to the blendings. For Ni X the 15.838 and 15.998nm lines are blended with Ni XIII lines. For Ni XII the 15.78nm line is blended with the two not completely resolved 15.753 and 15.773nm Ni XIII lines. Finally the blended 16.405 and 16.414nm Ni XIV lines are blended with the 164.17nm Ni XIII line.

Contrary to the case of figure 14 the recalculted single ion spectra are depending on the individual simulation, since from the previous section we know that relative ion abundances depend on the transport coefficients and on the rate coefficients. To have a quantitative idea of the contribution of the blending lines figures 15 and 16 are presented. In them examples of 'blended' single ion spectra are given for Ni X, Ni XII, Ni XIII and Ni XIV. In the former the three simulations 3 of figures 7, 9 and 13 are superposed, wheres in the latter the same is done the four simulations of figure 7. The normalisation line must be non-blended line, then are taken as normalisation line the 16.155-16.175 nm feature for Ni XIII and the 17.137nm line for Ni XIV. The contributions of the blending lines are not negligible, only for the 15.753-15.773nm Ni XIII blending the contribution of the Ni XII line is quite weak, It is then justified to use the Ni XIII blending as reference in analysing the Ni XIII spectra.

In the following figures experimental single ion spectra are compared with the corresponding simulations with blendings included. As a consequence of the discussion of the previous paragraph, individual simulations must be considered. The experimental spectra (dashed) are at the right wavelength, the simulated spectra (solid line) are displaced in wavelength to facilitate the visual comparison. Two simulated spectra are shown without and with blending contribution. They are

distiguishable at the blended wavelengths where obviously the 'blended' spectrum amplitude is larger. We consider the simulations 3 of figures 7, 9 and 13, respectively for divertor and limiter JET and for RFX.

6.I K-LIKE NIX

In figure 17 the Ni X spectra are shown (for RFX the Ni X feature around 14.5nm is too weak for a comparison). For this ion there was no problem with the energy levels and wavelenghts found in Refs [25-27]. The wavelengths are those from Shirai et al. [25]. The feature around 14.5 nm is well simulated in both cases, whereas for the two blended lines at longer wavelengths the limiter spectrum seems better. However we have to remember that in this figure (and this is valid also for the other ions to be discussed later) the normalisation is on the stronger component of the 14.5nm feature, whereas in the corresponding simulations shown in figures 7 and 9 the normalisation was from a best fit on five lines from different ions. There is no Ni XI spectrum, since only one strong line at 14.838 nm falls in the analysed wavelength range.

6.2 CL-LIKE NIXII

In figure 18 three Ni XII spectra are shown. Neglecting the line near 15.8 nm blended with Ni XIII, all three simulations are good and this is a good confirmation of the quality of our PECs. Concerning the 15.295 nm line, this line is found at the measured wavelength given by Fawcett [28] and confirmed in Ref. [11], but in the three Refs [25-27] the line is given at 15.3174nm. The emitting level of the latter line is $3p^4(^3P)\ ^3d\ ^2D_{3/2}$ and its value in cm^{-1} should become 677440 (83.992eV) instead of 676420. The energy of the lower $3p^5\ ^2P_{1/2}$ 23629 cm^{-1} is certainly correct. The wavelength of the other line from $3p^4\ (^3P)\ ^3d\ ^2D_{3/2}$ to the ground state should be 14.761nm, given in Ref. [28] as measured value.

6.3 S-LIKE NIXIII

In figure 19 three Ni XIII spectra are shown. Since the normalisation line at 15.753-15.773 nm is slightly affected by blendings, the experimental blue spectrum has been normalised to average of the red (with blendings) and green (without blendings) curves. In all cases the comparison between experiment and simulation seems good, except possibly for the weak feature around 16.2 nm. Ni XIII is the ion that was the most difficult to simulate

The line $3p^3\ (^4S)\ 3d\ ^3D_1$ - $3p^4\ ^3P_0$ is given in Refs [25-27] at 15.877nm and no line is definetly observed at this wavelength in all spectra. In Ref. [28] Fawcett gives for this transition a calculated value of 15.841nm In spite of the fact that also Fawcett gives the same measured value, we shifted the wavelength to his calculated value, then this Ni XIII line becomes blended with the 15.838nm Ni X line. The energy of the level $3p^3\ (^4S)\ ^3d\ ^3D_1$ should become in cm^{-1} 651330 instead of 649900.

A clear Ni line is observed at 16.222nm, which is not reported in any of the quoted references. From spectra with different line ratios between the 14.4–14.8 and 16.0-16.4 nm ranges, this line in amplitude correlates with either Ni XIII or NI XIV lines. We have identified it as the 4-41 transition in the Bhatia's paper [12], which is classified there as $3p^4\ ^1D_2 - 3p^3\ (^2D)\ 3d\ ^3P^1$. The lower level is

certainly $3p^4\ ^1D_2$, whereas, based on the hierarchy of oscillator strengths in our multi-configuration atomic structure calculations, we propose that the upper level should be classified as 3p3 (2D) 3d 1P1. This means that the designations for levels 39 and 41 in Ref. [12] should be switched. The energy for the level $3p^3$ (^{2}D) 3d $^1P_1$ becomes then 663480 cm^{-1}.

6.4 P-LIKE NIXIV

Only in the Jet limiter spectrum it is possible to analyse a single ion Ni XIV and this is shown in figure 20 upper. Since the strong 16.41 feature is blended with a Ni XIII line, the Ni XIV spectra are normalised the 'mean' of the lines at 16.969 and 17.137nm. Concerning line wavelengths and energy levels, the PEC calculations show near the 16.414 $3p^2$ (^{3}P) 3d $^2F_{7/2}$ - $3p^3\ ^2D_{5/2}$ transition another nearby strong line $3p^2$ (^{3}P) 3d $^2F_{5/2}$ - $3p^3\ ^2D_{3/2}$ not found in Refs [25-28]. We give to this transition a wavelength equal to 16.405 nm (blended then with the other indicated transition, given the 0.02 nm spectrometer resolution), supposing the $\Delta\lambda$ calculated by Fawcett [30] equal to 0.0096 nm is correct, this being probably a superior limit, since for the corresponding iron transitions Fawcett gives $\Delta\lambda$s calculated and measured, respectively, equal to 0.0124 and 0.0024 nm. The upper level energy is 655340 cm^{-1}.

For Ni XIV all the remaining non Ni lines are identified in the Jet report [16] as being (in nm) O V 16.80, C VI Ly-alfa*5 16.868, O V 17.022 and O VIII 17.08 (the latter rather proposed than identified) and the strong O V 17.217

6.5 SI-LIKE NIXV

The JET limiter Ni XV spectrum is shown in the figure 20 (lower) normalised to the 17.927nm line. Concerning wavelengths, the only remark is that the same line is given in Ref.[25] at 17.674nm and in Ref.[27] at 17.670nm and the latter value is clearly the right one. We think for this ion too the agreement betweeen predictions and experiments is satisfactory even if the simulated 17.373 nm line is weaker than the experimental line and no blending line from another element present in JET plasmas has been found.

CONCLUSION

Experimental M-shell nickel spectra in the 14.4-18.0nm region from the JET tokamak (both on divertor and limiter configurations) and from the reversed field pinch RFX have been simulated. These spectra include lines from five ionisation states, namely from Ni^{10+} K-like to Ni^{14+} Si-like ions. Collisional Radiative (CR) models have been constructed for these six Ni ions, using atomic data generated from *ab initio* atomic structure calculations with the Hebrew University Lawrence Livermore Atomic Codes (HULLAC). Electron collisional excitation and radiative decay are the populating processes of the excited states. These models give photon emission coefficients (PECs) for the emitted lines at electron density and temperature values corresponding to the experimental situations in MCF devices.

The wavelengths and energy levels involved in the transitions included in the CR model are

given in Appendix B, taking assessed spectral data in the Monograph by Shirai et al. [25]. For a few energy levels there was not agreement with the experimental data, the required corrections are given, being discussed in the section on the single ionisation degree spectra spectra.

Impurity modelling is performed using a 1-D impurity transport code, calculating the steady state radial distribution of the Ni ions. The code describes ionisation, recombination and radial transport of the ions of a given impurity species. It requires as input data the radial profiles of $T_e(r)$ and of $n_e(r)$, needed to evaluate the ionisation and recombination rate coefficients, and two transport coefficients (a diffusion coefficient D(r) and a convection velocity V(r).

Two sets of ionisation and recombination rate coefficients have been tested, It appears that the ionisation rate coefficients calculated by Pindzola et al. [32] and the recombination rates previously used in our code [34] give a better representation of the reported experimental data on M-shell Ni spectra. Fitting paramters to evaluate the DR rate coefficients for low ionisation Ni ions (up to recombining Al-like Ni^{15+} ions) are given in Appendix C.

The Ni line brightnesses are evaluated in a post-processing subroutine and simulated spectra are obtained. Difficulties were faced to get a satisfactory simulation of the experimental data. As described in the previous paragraphs, these are related to the low ionisation degree of the involved ions and to the fact that in Tokamak plasmas their emitting shells are located in the extreme periphery.

For each simulation the best fit is done on the peaks of the strongest lines of the Ni ionisation degrees contributing to the features of the detected spectra. The 'best' spectra are the ones with the lowest estimated sample deviation at the spectral peaks. For each experimental spectrum a few simulations are presented, since a unique choice has not been found by selecting the input parameters of the transport code.

The partial spectra corresponding to a single ionisation degree, in absence of blendings, depend only of the T_e and n_e values in the emitting shells of the ionisation states considered. On the other hand, the superposition of the these spectra depends on the experimental conditions, as a consequence of the fact that the ion charge distribution depends not only on the radial profiles of Te and ne, but also on the chosen ionisation and recombination rate coefficients and on the radial profiles.

The single ionisation degree spectra are then compared with the predictions. For the considered ne range the PECs can be considered independent of n_e. There is a their T_e dependence, but it is much reduced when considering line ratios and the spectral fits done are actually a comparison of line ratios. The influence of line blendings on the single ionisation degree spectra has been considered. The global agreement found between experimental and simulated single ionisation degree spectra give confidence on the atomic data used to build the required CR models.

APPENDIX A

In this Appendix we compare the Hullac PECs for Ni XII and Ni XIII with the ones reported, respectively, in Refs [11] and [12].

In the former three Ni XII line ratios (R_1, R_2 and R_3) are used for the analysis of the JET spectra.

With respect to the sum of the PECs of the line blend at 15.215nm they are, respectively, the PECs of the line at 15.417, 15.295 and 16.055nm.

In the figures of Ref. [11] curves of the three line ratios are given only for $n_e. \leq 0.5\ 10^{18}\ m^{-3}$, the authors stating that above $0.5\ 10^{18}\ m^{-3}$ the line ratios are independent of ne. The Hullac calculations indicate that between $1\ 10^{18}$ and $.3\ 10^{20}\ m^{-3}$ the ratios R_1 and R_3 are practically independent of n_e. The ratio R_2, on the other hand, increases from ~0.42 at $n_e.= 1.\ 10^{18}\ m^{-3}$ to ~0.44-0.46 at $n_e.\geq 3\ 3.10^{18}\ m^{-3}$. In the table the Hullac line ratios at $n_e.\geq 3\ 3.e^{18}\ m^{-3}$ are compared for two T_e values (50 and 150eV) with those at $ne.3\geq 5.e^{17}\ m^{-3}$ from Ref. [11]. For R_1 and R_3 there is good agreement, whereas for R_2 the values of Ref. [11] are ~20% larger. But it must be pointed out that our line ratios reduce for R_2 the discrepancy between experiment and theory of table 2 of Ref. [11]

	Hullac	Ref. [11]	Modified	Hullac	Ref. [11]	Modified
T_e (eV)	50	50	50	150	150	150
R_1	0.579	0.56	058/0.58	0.576	0.54	0.57/0.57
R_2	0.454	0.55	0.51/0.53	0.441	0.56	0.49/0.49
R_3	0.280	0.30	0.29/0.29	0.254	0.28	0.26/0.26

As stated in section 3, we have compared our DWA collision rates for NiXII with the recent *R*-matrix data of Matthews et al. [24]. The comparison is in the column 'modified' of the Table. There are two numbers in the column for each temperature, the first is the ratio at $5\ 10^{17}\ m^{-3}$, the second is the ratio at $3\ 10^{20}\ m^{-3}$. There is almost no density sensitivity at all in this range. For R1, the inclusion of the Matthews data [24] has almost no effect on the ratio and keeps us close to Keenan's values [11]. For R_2, the modified data increases the ratio by about 10% and brings us close to Keenan's value [11]. For R_3, there is almost no effect. R_2 is the only ratio that has a different lower level ($^2P_{1/2}$ instead of the ground $^2P_{3/2}$) for the transition in the numerator. What we can see is that by putting in the R-matrix 1-2 collision rate (which is between 6 and 10 times larger than the Hullac value for the transition $^2P_{3/2}$- $^2P_{1/2}$), we get only a small effect.

A final point concerning Ni XII: Keenan et al. [11] did some test calculations where they just "made-up" proton excitation rates equal to and 10× the electronimpact fine structure rates; they found no important effects due to the proton impact "data".

Between the tables of Ref. [12], the only one we can compare with is table VA, where the product $P_{j,i}\ N_e = n_j\ A_{j,i}$ (see formula (1)) is tabulated for many Ni XIII lines for $n_e = 1e^{18}\ m^{-3}$ and T_e = 170eV with proton excitation between the lowest five $3s^23p^4$ (^3P, ^1D, ^1S) levels. Comparing the fractional level populations of these five low levels given in tables IVA and IVB of Ref. [12], it appears that only the ^1S fractional population is noticeably affected (50% increase) by proton collisions. Between upper $3s^23p^33d$ levels of the considered lines only the level 47 ^1P shows a 40% increase with proton collisions. We compare our calculated values with and without proton collisions (for $n_e = 1e^{18}\ m^{-3}$ and $T_e = 150$eV) with table VA of Ref. [12] getting:

line levels	λ [nm]	Hullac	Ref. [10]	Hullac w/ Protons
1 – 38	16.417	1.48e3	1.66e3	1.38e+03 (-7%)
1 – 42(41)	15.773	2.41e3	2.37e3	2.22e+03 (-8%)
1 – 43	15.512	2.31e3	2.20e3	2.32e+02 (<1%)
2 – 43	15.997	9.95e2	1.15e3	1.00e+03 (<1%)
3 – 44	15.841	4.15e3	4.88e3	4.22e+02 (+2%)
4 – 41(42)	16.222	4.78e2	6.48e2	5.15e+02 (+8%)
4 – 45	16.155	7.43e2	7.43e2	7.91e+02 (+6%)
4 – 46	15.753	1.23e3	1.59e3	1.32e+03 (+7%)
5 – 47	16.175	3.04e2	3.86e2	5.30e+02 (+74%)

[note there is an inversion for the levels 41 and 42 between Ref. [12] and Hullac (index between the brackets)].

Except for the line 4-41 (one of the weaker lines in this set) the differences are–£ 20% and then the comparison has to be considered as good. Having included the proton excitation data from [10] in our CR models, we find that PECs for transitions ending on levels 2, 3 and 4 are enhanced by less than 10%, indicating that the proton-impact excitation have only a small effect. For the PEC for the λ = 16.175nm transition, which ends on the 1S level (level 5), we find a 74% enhancement of the value from our Hullac-based model; this is the weakest PEC among the considered transitions and need not trouble us further

APPENDIX B

Wavelengths in nm, lower and upper energy levels in cm, lower and upper configurations. Used are the assessed spectral data given in the Monograph by by Shirai et al. [25], unless specified by a star. For these line the modifications are explained in section 6, when discussing the corresponding single ionisation spectrum.

NI X

1	*14.4216*	*0*	*693404*	$3p^6\ 3d\ ^2D_{3/2}$	$3p^5\ (^2P)\ 3d^2\ (^3F)\ 3d\ ^2D_{3/2}$
2	*14.4323*	*0*	*692890*	$3p^6\ 3d\ ^2D_{3/2}$	$3p^5\ (^2P)\ 3d^2\ (^3F)\ 3d\ ^2D_{5/2}$
3	*14.4880*	*3178*	*693404*	$3p^6\ 3d\ ^2D_{5/2}$	$3p^5\ (^2P)\ 3d^2\ (^3F)\ 3d\ ^2D_{3/2}$
4	*14.4988*	*3178*	*692890*	$3p^6\ 3d\ ^2D_{5/2}$	$3p^5\ (^2P)\ 3d^2\ (^3F)\ 3d\ ^2D_{5/2}$
5	*14.5061*	*0*	*689365*	$3p^6\ 3d\ ^2D_{3/2}$	$3p^5\ (^2P)\ 3d^2\ (^3F)\ 3d\ ^2P_{3/2}$
6	*14.5733*	*3178*	*689365*	$3p^6\ 3d\ ^2D_{5/2}$	$3p^5\ (^2P)\ 3d^2\ (^3F)\ 3d\ ^2P_{3/2}$
7	*14.6081*	*0*	*684552*	$3p^6\ 3d\ ^2D_{3/2}$	$3p^5\ (^2P)\ 3d^2\ (^3F)\ 3d\ ^2P_{1/2}$
8	*15.8377*	*3178*	*634583*	$3p^6\ 3d\ ^2D_{5/2}$	$3p^5\ (^2P)\ 3d^2\ (^3F)\ 3d\ ^2D_{7/2}$
9	*15.9977*	*0*	*695091*	$3p^6\ 3d\ ^2D_{3/2}$	$3p^5\ (^2P)\ 3d^2\ (^3F)\ 3d\ ^2F_{5/2}$
10	*16.0794*	*3178*	*625091*	$3p^6\ 3d\ ^2D_{5/2}$	$3p^5\ (^2P)\ 3d^2\ (^3F)\ 3d\ ^2F_{5/2}$

NI XI

	1	14.8377	0	673960	$3p^6\ ^1S_0$	$3p^5\ 3d^2\ ^1P_1$

NI XII

*	1	14.7610	0	677440	$3p^5\ ^2P_{3/2}$	$3p^4\ (^3P)\ 3d^2\ ^2D_{3/2}$
	2	15.2151	0	657290	$3p^5\ ^2P_{3/2}$	$3p^4\ (^3P)\ 3d^2\ ^2D_{3/2}$
	3	15.2153	0	657230	$3p^5\ ^2P_{3/2}$	$3p^4\ (^3P)\ 3d^2\ ^2D_{3/2}$
*	4	15.295	23629	677440	$3p^5\ ^2P_{1/2}$	$3p^4\ (^3P)\ 3d^2\ ^2D_{3/2}$
	5	15.4171	0	648670	$3p^5\ ^2P_{3/2}$	$3p^4\ (^3P)\ 3d^2\ ^2D_{3/2}$
	6	15.7795	23629	657290	$3p^5\ ^2P_{1/2}$	$33p^4\ (^3P)\ 3d^2\ ^2D_{3/2}$
	7	16.0556	0	622840	$3p^5\ ^2P_{1/2}$	$3p^4\ (^3P)\ 3d^2\ ^2D_{3/2}$
*	8	16.688	23629	622840	$3p^5\ ^2P_{3/2}$	$3p^5\ (^2P)\ 3d^2\ (^3F)\ 3d\ ^2D_{7/2}$

NI XIII

	1	15.5120	0	644660	$3p^4\ ^3P_2$	$3p^3\ (^4S)\ 3d\ ^3D_2$
	2	15.7532	47032.9	681820	$3p^4\ ^1D_2$	$3p^3\ (^2D)\ 3d\ ^1F_3$
	3	15.7732	0	633990	$3p^4\ ^3P_2$	$3p^3\ (^4S)\ 3d\ ^3D_3$
*	4	15.841	20060.	651330	$3p^4\ ^3P_0$	$3p^3\ (^4S)\ 3d\ ^3D_1$
	5	15.997	19541.8	644660	$3p^4\ ^3P_1$	$3p^3\ (^4S)\ 3d\ ^3D_2$
	6	16.1547	47032.9	666050	$3p^4\ ^1D_2$	$3p^3\ (^2D)\ 3d\ ^1D_2$
	7	16.1752	97836.2	716070	$3p^4\ ^1S_0$	$3p^3\ (^2P)\ 3d\ ^1P_1$
*	8	16.222	47032.9	663480	$3p^4\ ^1D_2$	$3p^3\ (^2D)\ 3d\ ^1P_1$
	9	16.4172	0	609120	$3p^4\ ^3P_2$	$3p^3\ (^2D)\ 3d\ ^3P_2$

NI XIV

*	1	16.405	45767.8	655340	$3p^3\ ^2D_{3/2}$	$3p^2\ (^3P)\ 3d\ ^2F_{5/2}$
	2	16.4146	53569.0	662770	$3p^3\ ^2D_{5/2}$	$3p^2\ (^3P)\ 3d\ ^2F_{7/2}$
	3	16.480	85126.7	691930	$3p^3\ ^2P_{1/2}$	$3p^2\ (^3P)\ 3d\ ^2D_{3/2}$
	4	16.812	0.	594810	$3p^3\ ^4S_{3/2}$	$3p^2\ (^3P)\ 3d\ ^4P_{1/2}$
	5	16.837	96630.	690560	$3p^3\ ^2P_{3/2}$	$3p^2\ (^3P)\ 3d\ ^2D_{5/2}$
	6	16.969	0.	589310	$3p^3\ ^4S_{3/2}$	$3p^2\ (^3P)\ 3d\ ^4P_{3/2}$
	7	16.988	45767.8	634430	$3p^3\ ^2D_{3/2}$	$3p^2\ (^1D)\ 3d\ ^2D_{5/2}$
	8	17.050	45767.8	632280	$3p^3\ ^2D_{3/2}$	$3p^2\ (^1D)\ 3d\ ^2D_{3/2}$
	9	17.137	0.	583530	$3p^3\ ^4S_{3/2}$	$3p^2\ (^3P)\ 3d\ ^4P_{5/2}$
	10	17.216	53569.	634430	$3p^3\ ^2D_{5/2}$	$3p^2\ (^1D)\ 3d\ ^2D_{5/2}$
	11	17.728	96630.	660710	$3p^3\ ^2P_{3/2}$	$3p^2\ (^1D)\ 3d\ ^2P_{3/2}$
	12	17.756	85126.7	648320	$3p^3\ ^2P_{1/2}$	$3p^2\ (^1D)\ 3d\ ^2P_{1/2}$

NI XV

1	*17.3724*	*62852.1*	*638477*	$3p^2\ ^1D_2$	$3p\ 3d\ ^1F_3$
2	*17.499*	*14917.5*	*586379*	$3p^2\ ^3P_1$	$3p\ 3d\ ^3D_2$
3	*17.610*	*14917.5*	*582760*	$3p^2\ ^3P_1$	$3p\ 3d\ ^3D_1$
4	*17.670*	*0.*	*565930*	$3p^2\ ^3P0$	$3p\ 3d\ ^3P_1$
5	*17.8779*	*14917.5*	*574267*	$3p^2\ ^3P_1$	$3p\ 3d\ ^1D_2$
6	*17.8890*	*27376.5*	*586379*	$3p^2\ ^3P_2$	$3p\ 3d\ ^3D_2$
7	*17.9273*	*27376.5*	*585185*	$3p^2\ ^3P_2$	$3p\ 3d\ ^3D3$
8	*18.006*	*27376.5*	*582760*	$3p^2\ ^3P_2$	$3p\ 3d\ ^3D_1$
9	*18.4884*	*14917.5*	*555797*	$3p^2\ ^3P_1$	$3p\ 3d\ 3P_2$

APPENDIX C

The DR rate coefficients α_{drZ} obtained in Ref. [34] using the Burgess-Merts formula have been fitted with the following formula

$$\alpha_{drZ} = \frac{1}{T_e^{3/2}} \sum_{i=1}^{2} c_i \exp\left(-\frac{E_i}{T_e}\right)$$

where T_e and E_i are in eV, ad in cm^3/s and c_i in $cm^3\ eV^{1.5}$ /s. Z is the charge of the recombining ion. The coefficients c_i and E_i for recombining Co-like (Z=1) to Al-like (Z=15) Ni ions are given below

Z	C_1	C_2	E_1	E
1	1.24e-09		13.8	
2	7.55e-09		22.7	
3	2.52e-08		35.9	
4	5.79e-08		42.0	
5	9.58e-08		51.1	
6	1.45e-07		51.6	
7	2.13e-07		56.1	
8	2.88e-07		64.6	
9	3.87e-07		72.7	
10	1.24e-07	5.69e-07	169.0	74.7
11	5.84e-07	1.25e-07	70.3	180.0
12	1.47e-07	4.56e-07	186.0	69.4
13	3.12e-07	2.73e-07	55.0	140.0
14	2.63e-07	1.79e-07	48.6	145.0
15	2.76e-07	8.80e-08	45.7	174.0

REFERENCES

[1]. De Michelis C and Mattioli M 1984 *Rep. Prog Phys.* **47** 1233

[2]. Bitter M, Hsuan H, Hill K W and Zarnstorff M 1993 *Phys. Scripta* **T47** 87

[3]. Mattioli M, Fournier K, Carraro L et al 2000 *Phys. Rev*. E **60** 4760

[4]. Mattioli M,. Fournier K,. Carraro L et al 2001 *J. Phys B: At. Mol. Opt. Phys.* **34** 127

[5]. Mattioli M,. Fournier K., Puiatti M E et al 2002 *Plasma Phys Control. Fusion* **44** 33

[6]. Fournier K B, Finkenthal M, Pacella D et al. 2000 «Tokamak Spectroscopy for X-Ray Astronomy» Proc. of the Workshop on Atomic Data Needs for X-ray Astronomy, NASA-CP-2000-209968 (Bautista M,. Kallman T and Pradhan A editors), page 127 (also:http://heasarc.gsfc.nasa.gov/docs/heasarc/atomic)

[7]. Fournier K B, May M J, Liedahl D A et al 2001 *Astrophys. J*. 561 1144

[8]. Mauche, C W, Liedahl, D A and Fournier, K B 2003 *Astrophys. J.* to appear (see also http://arXiv.org/abs/astro-ph/0304080)

[9]. Brickhouse, N S and Dupree, A K 1998 *Astrophys. J.* **502**, 918

[10]. Fournier K B, Finkenthal M, Pacella D et al 2001 *Astrophys. J*. 550 L117

[11]. Keenan F P, Botha G J, Matthews A et al 2001 *J. Phys B: At. Mol. Opt. Phys.* **34** 639

[12]. Bhatia A K, and Doschek G A 1998 *At. Data Nucl. Data Tables* 68 49

[13]. Schwob J L, Wouters A. W, Suckewer S and Finkenthal M 1987 *Rev. Sci. Insrum.* **58** 1601

[14]. Beurskens M N, Giovannozzi E, Gunn J et al 2001 *Proc. 28*th EPS Conf. *on Control. Fusion and Plasma Phys. (Funchal)* 25A 1229

[15]. Kallenbach A, Andrew Y, Beurskens M N et al 2001 *Proc. 29*th EPS Conf. on Control. Fusion and Plasma Phys. (Montreuxl) 26B O-3.22

[16]. Saoutic B, Ramette J, Mattioli M et al 1987 Jet Laboratory Report JETR(87) 14 (unpublished)

[17]. The JET Team, presented by Stott P E 1989 *J. Nucl. Mater.* 162-164 3

[18]. Carraro L, Costa S, Puiatti M E et al 2000 *Plasma Phys. Control. Fusion* **42** 731

[19]. Fournier K B 1998 *At. Data Nucl. Data Tables* **68** 1

[20]. Bar-Shalom A and Klapisch M 1988 *Comput. Phys. Commun.* **50** 375

[21]. Klapisch M 1971 *Comput. Phys. Commun.* **2** 239.

[22]. Klapisch M, Schwob J L, Fraenkel B and Oreg J 1977 *J. Opt. Soc. Am.* **67** 148

[23]. Bar-Shalom A, Klapisch M and Oreg J 1988 *Phys. Rev. A* **38** 1773

[24]. Matthews A, Ramsbottom C A, Bell K L and Keenan F P (1998) *At. Data Nucl. Data Tables* **70** 41, also, Matthews A. et al (1998) *Astrophys. J.* **492** 415

[25]. Shirai T, Sugar J, Musgrove A and Wiese W L. 2000 J. Phys. Chem. Ref. *Data Monograph No 8*, published by the American Institute of Physics and National Institute of Standard and Technology.

[26]. National Institute of Standards and Technology (NIST) Atomic Spectra Database http://aeldata.nist.gov

[27]. Kelly R J http://cfa-www.harvard.edu/amdata/ampdata/kelly/kelly.html

[28]. Fawcett B C 1987 *At. Data Nucl. Data Tables* **36** 151
[29]. Fawcett B C 1986 *At. Data Nucl. Data Tables* **35** 185
[30]. Fawcett B C 1986 *At. Data Nucl. Data Tables* **35** 203
[31]. Mazzotta P, Mazzitelli G, Colafrancesco S and Vittorio N, 1998 *Astron. Astrophys. Suppl. Series* **133**, 403
[32]. Pindzola M S, Griffin D C, Bottcher C et al 1991 *Phys. Scripta* T37 35
[33]. Cherkani-Hassani S, Khouilid M and Defrance P 2001 1991 *Phys. Scripta* T92 287
[34]. Mattioli M 1988 Cadarache Laboratory Report EUR-CEA-FC 1346 (unpublished).
[35]. Puiatti M E, Mattioli M, Telesca G et al 2002 *Plasma Phys. Contrl. Fusion* **44** 1863
[36]. Lawson K, Lauro-Taroni L, Giannella R et al. Jet Laboratory Report JET-P(99) 03 (unpublished)

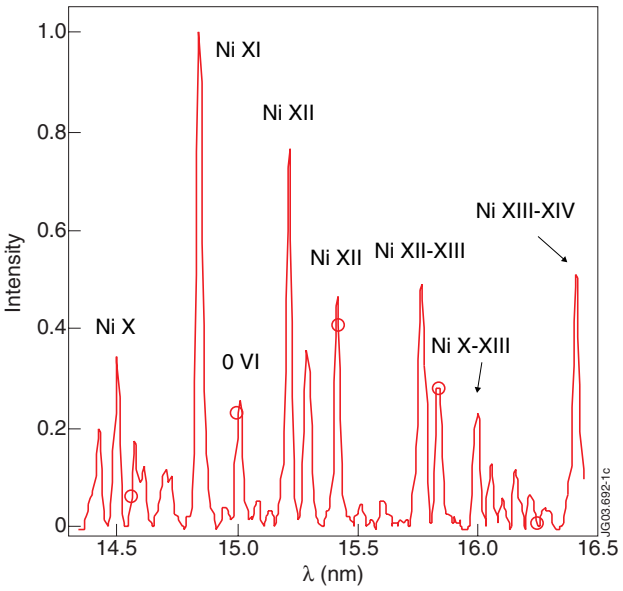

Figure 1: Experimental JET divertor spectrum between 14.3 and 16.5nm, normalised line to the 14.84nm Ni XI line, the most important lines (including the non Ni lines) are indicated with their spectroscopic notations.

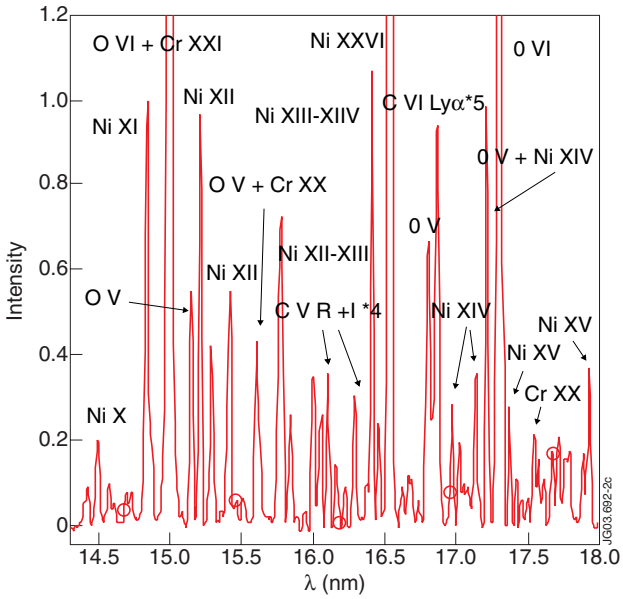

Figure 2: Same as figure 1 for a JET limiter spectrum, but towards the res the spectrum extends up to 18nm.

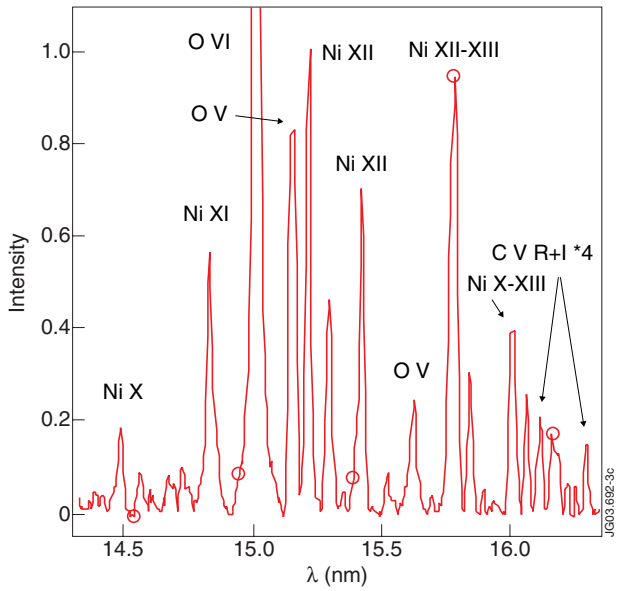

Figure 3 Same as figure 1 for a RFX spectrum, normalised to the 15.215nm Ni XII line.

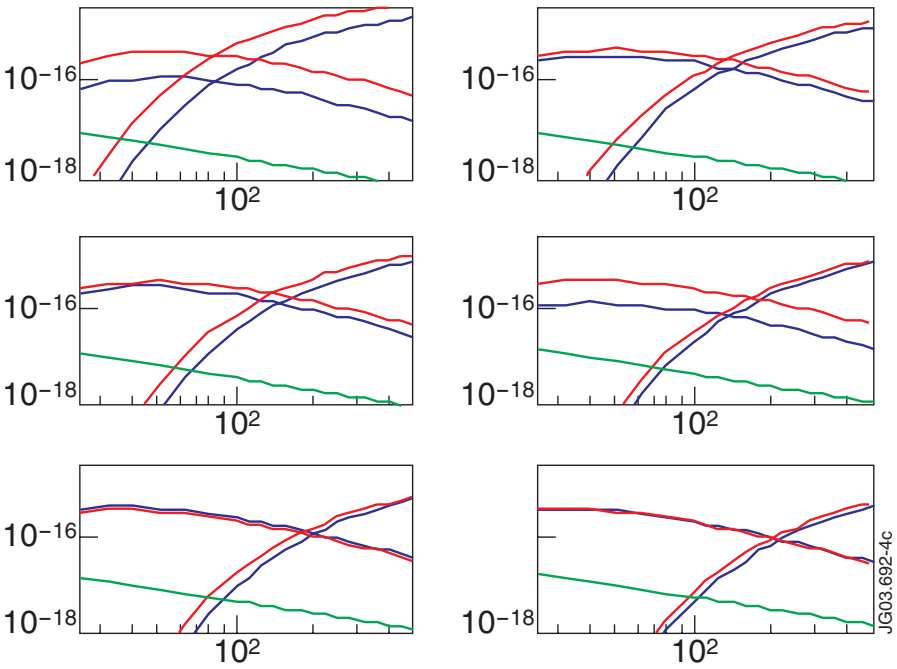

Figure 4: Rate coefficients (m^3/s) as function of T_e (eV) from Ni^{9+} to Ni^{14+} (from left to right and from top to bottom The rate coefficients for ionisation Sion, increasing as function of T_e, are from Ref. [31] (blue solid) and from Ref.[32] (red dashed), the rate coefficients for for dielectronic recombination α_{DR} are from Ref. [31] (blue solid) and from Ref.[33] (red dashed). The green curves show the rate coefficients for radiative recombination α_R from Ref.[31], for all considered ions they are much lower than the corresponding DR values.

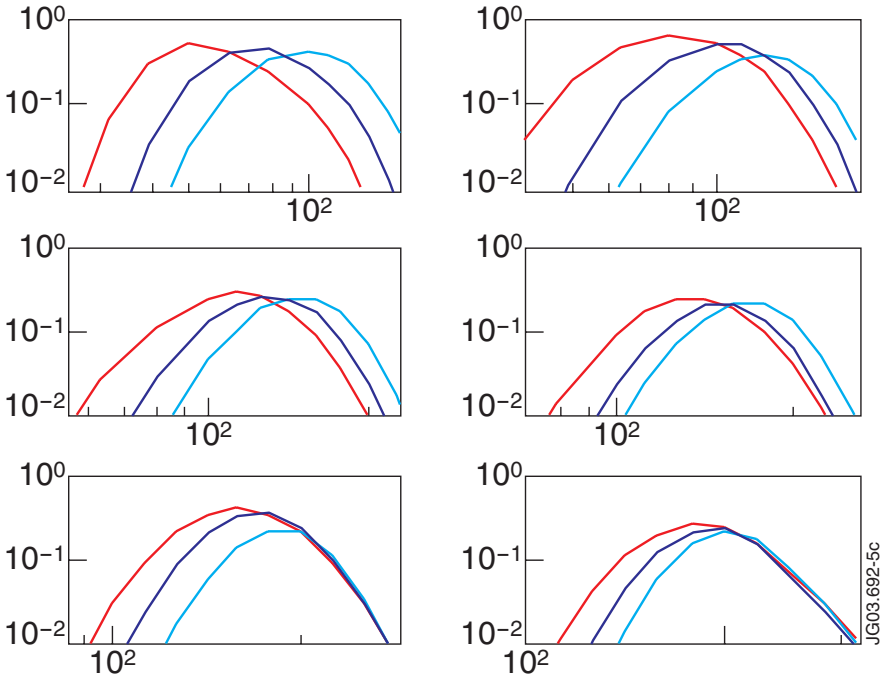

Figure 5: Fractional abundance curves for the same ions as in figure 4 using various proposed data for the rate coefficients. Blue curves: Sion and α_{DR} from Ref. [31]; red curves: Sion from Ref. [32] and α_{DR} from Ref. [31]; green curves: S_{ion} from Ref. [32] and α_{DR} from Ref. [33]; cyan curves: Sion from Ref. [31] and α_{DR} from Ref. [33].

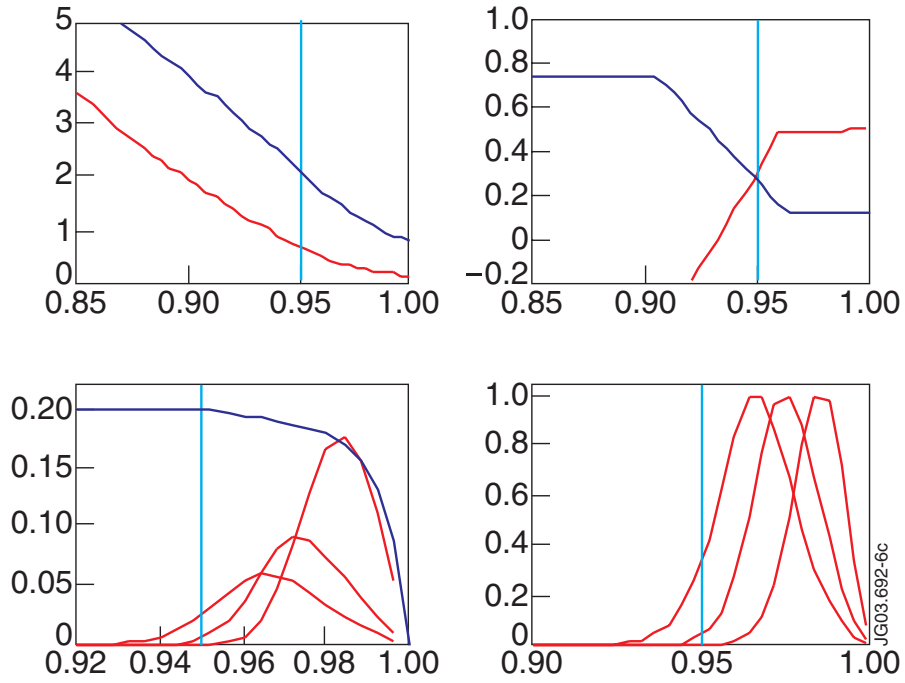

Figure 6: Transport simulation for the JET divertor plasma. Peripheral radial profiles of (a) n_e (blue solid line 10^{19} m^{-3}) and T_e (red dashed line 500eV), obtained by fitting the experimental data; (b) peripheral diffusion coefficient D (m^2/s) and inward convection velocity V (m/s), blue solid and red dashed line, respectively); (c) Ni ion densities n_z, normalized to the total Ni ion density (blue solid line /5); charge states from Nir^{9+} to Ni^{15+} red curves alternatively solid and dashed; (d) emissivities (normalised) E_{nor} of the strongest components of the experimental features of Fig. 1 from Ni X to Ni XV (alternatively red solid and dashed lines). The vertical cyan lines give the position of the LCFS at r=0.95m.

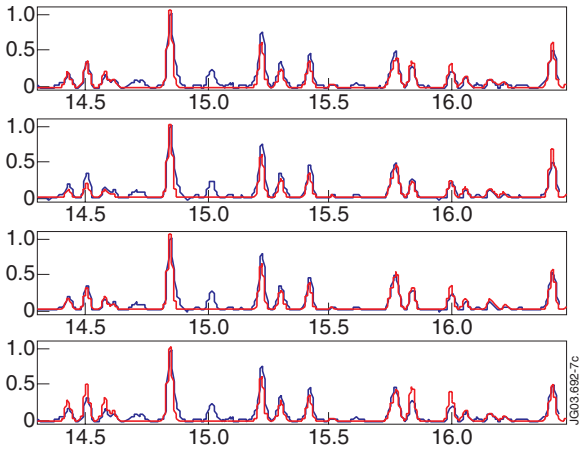

Figure 7: Normalised experimental JET divertor spectra (blue solid lines) and best fitted simulated spectra (red dashed lines) between 14.3 and 16.5 nm. From top to bottom : a) Sion and α_{DR} from Ref. [31]; b) S_{ion} from Ref. [32] and α_{DR} from Ref. [31]; c) S_{ion} from Ref. [32] and α_{DR} from Ref. [33]; d): S_{ion} from Ref. [31] and α_{DR} from Ref. [33].

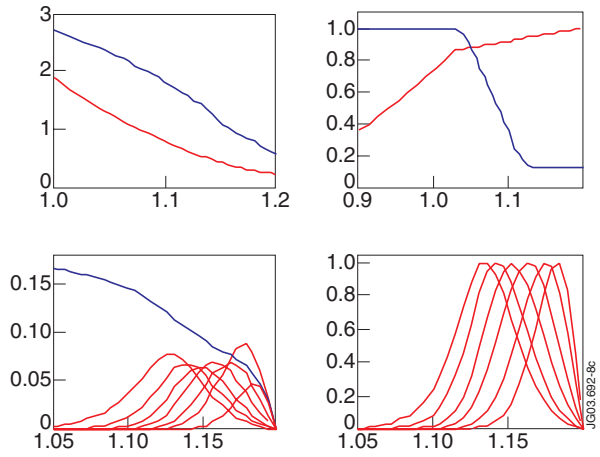

Figure 8: Same as figure 6 for the Jet limiter plasma with the following scales n_e 10^{19} m^{-3}, T_e 400 eV, D m^2/s and V $^2m/s$; normalised total Ni ion density /5.

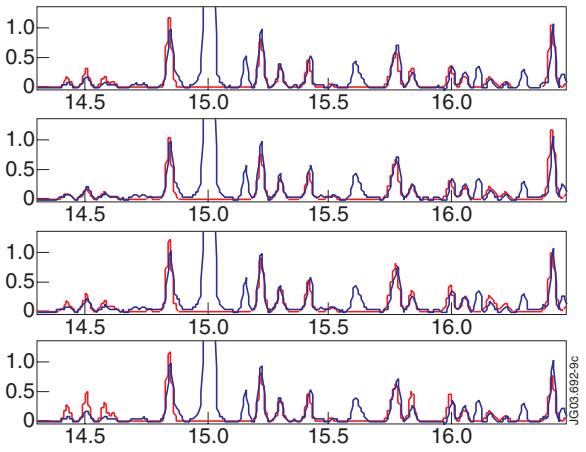

Figure 9: Same as figure 7 for the JET limiter plasma, best fitting of the simulated spectrum between 14.3 and 16.5nm.

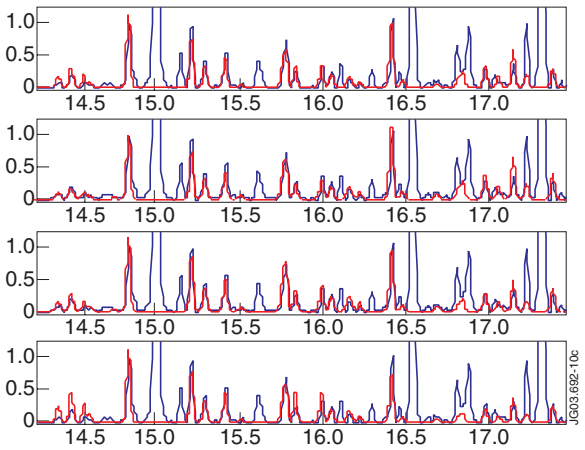

Figure 10: Same as figure 7 for the JET limiter plasma, best fitting of the simulated spectrum between 14.3 and 17.4nm.

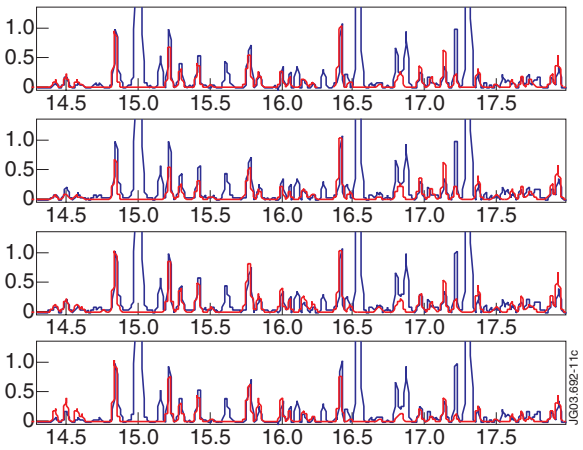

Figure 11: Same as figure 7 for the JET limiter plasma, best fitting of the simulated spectrum between 14.3 and 18.0nm.

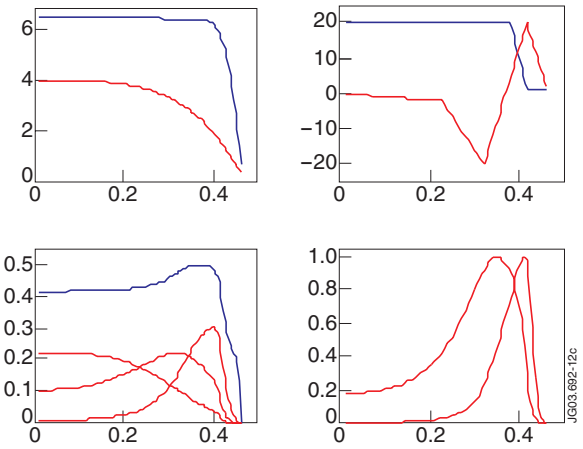

Figure 12: Same as figure 6 for the RFX plasma with the following scales n_e 10^{19} m^{-3}, T_e 50 eV, D m2/s and V 2ms; normalised total Ni ion density /2.

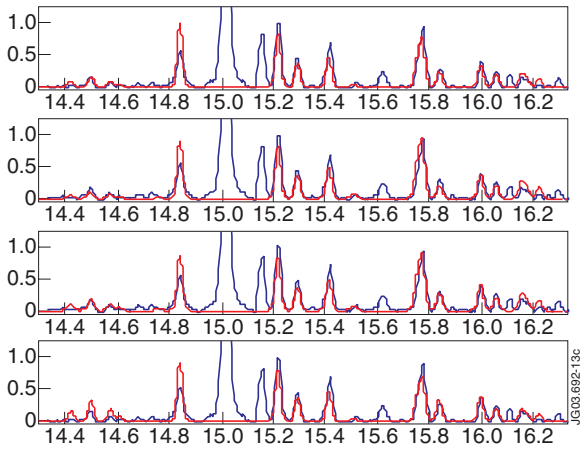

Figure 13: Same as figure 7 for the RFX plasma, best fitting of the simulated spectrum between 14.3 and 16.5nm.

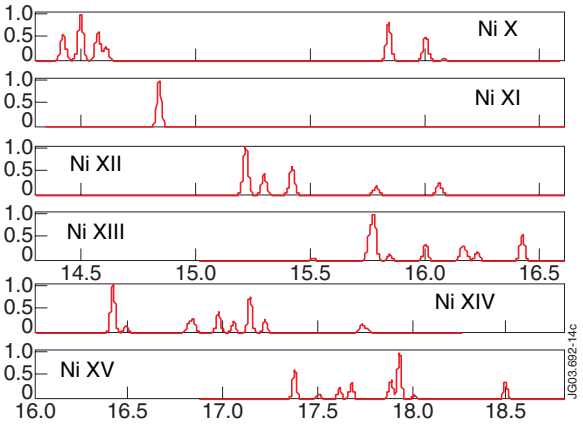

Figure 14:Normalised single ionisation degree Ni ion spectra (Ni X to Ni XV from top to bottom). Superposition of a few simulations of the three experimental conditions.

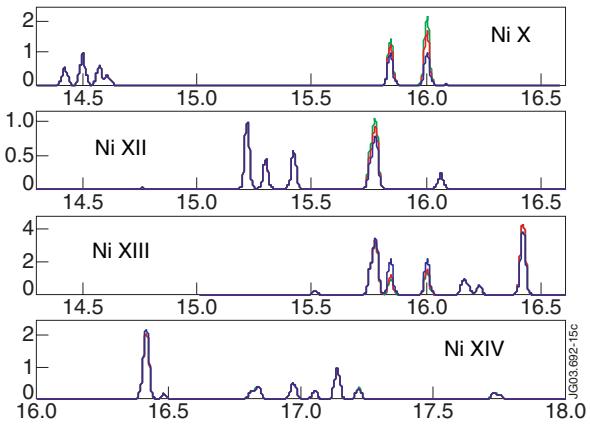

Figure 15: Same as figure 14 (from top to bottom Ni X-XII-XIII-XIV), but the blending contributions are added. The third simulations of figures 7, 9 and 13 are considered, respectively, blue, red and green lines.

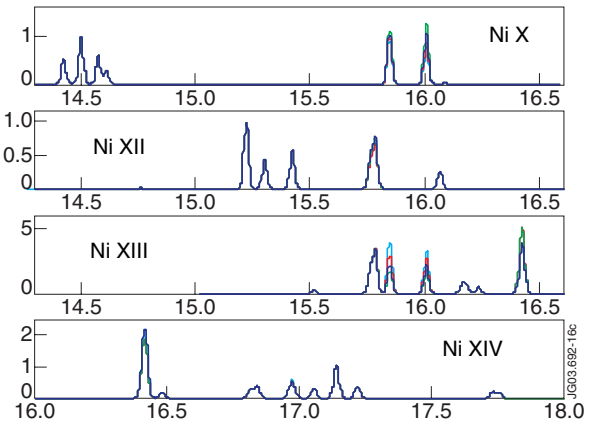

Figure 16: Same as figure 15. The four simulations of figure 7 are considered, respectively, blue, red, green and cyan lines.

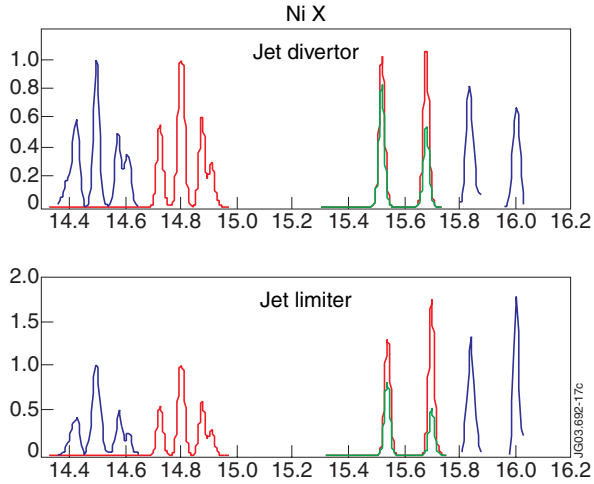

Figure 17: Experimental (blue dashed, displaced in wavelength) and simulated (red solid with blendings, green solid without blendings) Ni X spectra The simulated spectra (upper for JET divertor, lower for limiter plasma) correspond to the third simulatios of figure 7 and 9, respectively, i. e., with Sion from Ref. [32] and α_{DR} from Ref. [33]

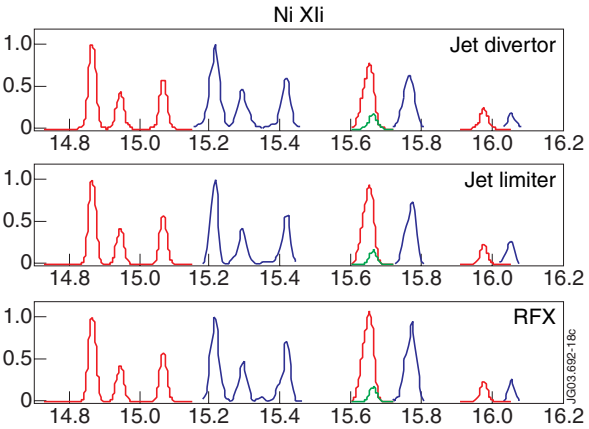

Figure 18: Same as figure 17 for Ni XII with (bottom) RFX spectrum added.

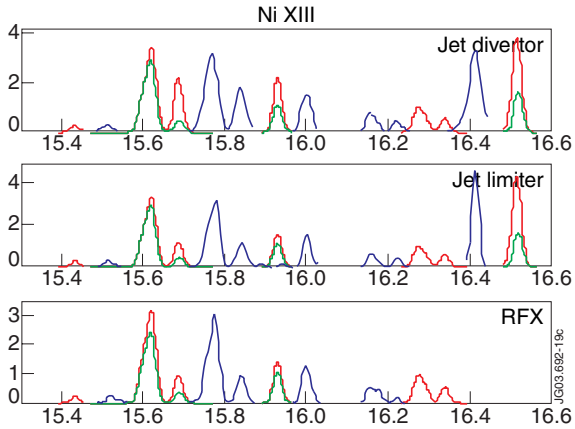

Figure 19: Same as figure 18 for Ni XIII. Since the normalisation line at 15.753-15.773nm feature is slightly affected by blendings, the experimental blue spectrum has been normalised to average of the red (with blendings) and green (wuthout blendings) curves.

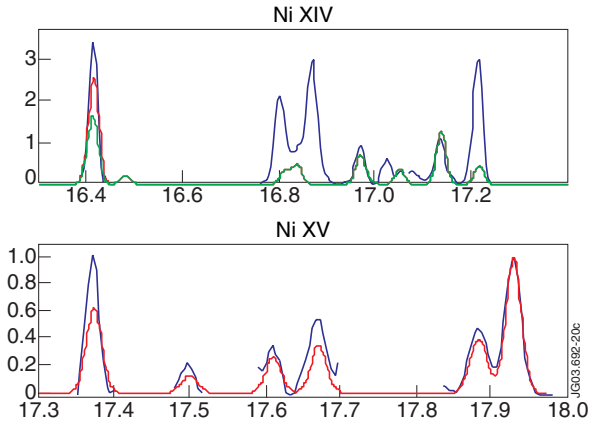

Figure 20: Same as previous three figures for Ni XIV (top) and Ni XV (bottom) for JET limiter plasma.